JACS
JOURNAL OF THE AMERICAN CHEMICAL SOCIETY
Communication
pubs.acs.org/JACS

3D Nitrogen-Doped Graphene Aerogel-Supported Fe_3O_4 Nanoparticles as Efficient Electrocatalysts for the Oxygen Reduction Reaction

Zhong-Shuai Wu,[†] Shubin Yang,[†] Yi Sun,[†] Khaled Parvez,[†] Xinliang Feng,*[,†,‡] and Klaus Müllen*[,†]

[†]Max-Planck-Institut für Polymerforschung, Ackermannweg 10, 55128 Mainz, Germany

[‡]School of Chemistry and Chemical Engineering, Shanghai Jiao Tong University, 200240, Shanghai, P. R. China

Supporting Information

ABSTRACT: Three-dimensional (3D) N-doped graphene aerogel (N-GA)-supported Fe_3O_4 nanoparticles (Fe_3O_4/N-GAs) as efficient cathode catalysts for the oxygen reduction reaction (ORR) are reported. The graphene hybrids exhibit an interconnected macroporous framework of graphene sheets with uniform dispersion of Fe_3O_4 nanoparticles (NPs). In studying the effects of the carbon support on the Fe_3O_4 NPs for the ORR, we found that Fe_3O_4/N-GAs show a more positive onset potential, higher cathodic density, lower H_2O_2 yield, and higher electron transfer number for the ORR in alkaline media than Fe_3O_4 NPs supported on N-doped carbon black or N-doped graphene sheets, highlighting the importance of the 3D macropores and high specific surface area of the GA support for improving the ORR performance. Furthermore, Fe_3O_4/N-GAs show better durability than the commercial Pt/C catalyst.

Catalysts for the oxygen reduction reaction (ORR) are key components of fuel cells.[1] Pt and its alloys remain the most efficient ORR catalysts, but the high cost and scarcity of Pt hamper further development of fuel cell technologies based on these materials. In this respect, a broad range of alternative catalysts based on nonprecious metals (Fe, Co, etc.)[2] or metal oxides (Fe_2O_3, Fe_3O_4, Co_3O_4, IrO_2, etc.)[3] as well as nitrogen-coordinated metal on carbon[4] and metal-free doped carbon materials[5] have been actively pursued. Metal or metal oxide catalysts frequently suffer from dissolution, sintering, and agglomeration during operation of the fuel cell, which can result in catalyst degradation.[6] To overcome this obstacle, nanostructured catalyst supports such as carbon (active carbon, porous carbon, carbon nanotubes, and graphene), metal, carbide, mesoporous silica, and conducting polymers have been developed to maximize the electroactive surface area of catalysts and improve their catalytic activity and durability.[6] Among these, graphene, a two-dimensional single-layer sheet of hexagonal carbon, has emerged as a new-generation catalyst support because of its excellent electrical conductivity, high surface area, good chemical and environmental stability, and strong adhesion to catalyst particles. Despite the tremendous progress in graphene-based catalysts for the ORR,[3e,7] there have been no reports of the controllable assembly of nonprecious metal oxide nanoparticles (NPs) supported on three-dimensional (3D) graphene networks as ORR catalysts. Such systems are attractive targets, as they would allow the utilization of the unique features of graphene sheets, such their as rich macroporosity and multidimensional electron transport pathways.

In this communication, we demonstrate Fe_3O_4/N-GAs, a novel class of monolithic Fe_3O_4 NPs supported on 3D N-doped graphene aerogels (N-GAs). The graphene hybrids show an interconnected macroporous framework of graphene sheets with uniform deposition of Fe_3O_4 NPs. In studying the effects of the carbon support on the Fe_3O_4 NP ORR catalyst, we found that Fe_3O_4/N-GAs exhibit a more positive onset potential, higher cathodic density, lower H_2O_2 yield, and higher electron transfer number for the ORR in alkaline media than Fe_3O_4 NPs supported on N-doped carbon black (Fe_3O_4/N-CB) or N-doped graphene sheets (Fe_3O_4/N-GSs). Additionally, Fe_3O_4/N-GAs show better durability than the commercial Pt/C catalyst.

The fabrication process for 3D Fe_3O_4/N-GAs is demonstrated in Figure 1. First, graphene oxide (GO) (Figure S1 in the Supporting Information)[8] was dispersed in water by sonication, reaching a concentration up to 1.5 mg mL^{-1}. Next, iron acetate (1−40 mg) and polypyrrole (PPy) (20 mg)

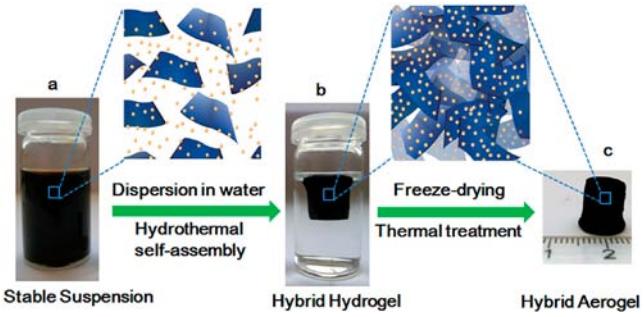

Figure 1. Fabrication process for the 3D Fe_3O_4/N-GAs catalyst. (a) Stable suspension of GO, iron ions, and PPy dispersed in a vial. (b) Fe- and PPy-supporting graphene hybrid hydrogel prepared by hydrothermal self-assembly and floating on water in a vial, and its ideal assembled model. (c) Monolithic Fe_3O_4/N-GAs hybrid aerogel obtained after freeze-drying and thermal treatment.

Received: March 29, 2012
Published: May 24, 2012

   dx.doi.org/10.1021/ja3030565 | J. Am. Chem. Soc. 2012, 134, 9082−9085

were slowly added to 6 mL of the GO dispersion to form a stable aqueous suspension (Figure 1a). Subsequently, these ternary components were hydrothermally assembled at 180 °C for 12 h to form a graphene-based 3D hydrogel (Figure 1b). In this way, Fe_3O_4 NPs could nucleate and grow on the graphene surface with simultaneous incorporation of nitrogen species into the graphene lattice. The as-prepared hydrogel was directly dehydrated via a freeze-drying process to maintain the 3D monolithic architecture and then heated at 600 °C for 3 h under nitrogen (Figure 1c). The final product from this process was a black monolithic hybrid aerogel composed of N-doped graphene networks and Fe_3O_4 NPs (see below).

The structure and morphology of as-prepared Fe_3O_4/N-GAs were investigated by means of X-ray diffraction (XRD), scanning electron microscopy (SEM) and transmission electron microscopy (TEM). The XRD pattern confirmed the formation of Fe_3O_4 (JCPDS no. 65-3107) in the hybrids (Figure 2a).[9] Remarkably, no apparent diffraction peak could be identified at 20−30°, indicating that Fe_3O_4 NPs were efficiently deposited on the graphene surface, suppressing the stacking of graphene layers. SEM images revealed an interconnected, porous 3D graphene framework with continuous macropores in the micrometer size range (Figure 2b,c). Apart from the decoration of Fe_3O_4 NPs on both sides of the graphene sheets (Figure 2c), it is noteworthy that a significant portion of the NPs (30% based on statistical analysis of the SEM images) are encapsulated within the graphene layers (Figure 2d), suggesting efficient assembly between the NPs and the graphene sheets. Such a geometric confinement of metal oxide NPs within graphene layers has been reported to enhance their interface contact and to suppress the dissolution and agglomeration of NPs, thereby promoting the electrochemical activity and stability of the hybrids.[10] TEM characterization further validated the uniform distribution of Fe_3O_4 NPs (with sizes of 20−80 nm) on the graphene (Figure 2e). High-resolution TEM (HRTEM) revealed a typical Fe_3O_4 NP with a well-crystalline texture that was entirely encapsulated by graphene sheets (≤6 layers; Figure 2f). Brunauer−Emmett−Teller (BET) analysis showed that a specific surface area of 110 m^2 g^{-1} for Fe_3O_4/N-GAs together with meso- and macroporous features can be obtained (Figure S2). The content of Fe_3O_4 in Fe_3O_4/N-GAs (46.2 wt %) was further confirmed by thermogravimetric analysis (TGA) (Figure S3).

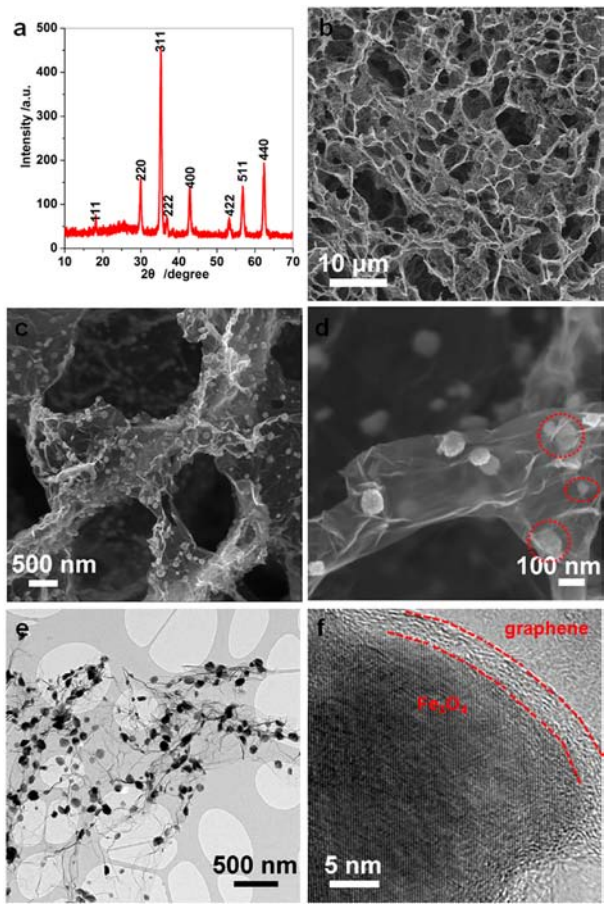

Figure 2. Structure and morphology of Fe_3O_4/N-GAs catalysts. (a) XRD pattern and (b−d) typical SEM images of Fe_3O_4/N-GAs revealing the 3D macroporous structure and uniform distribution of Fe_3O_4 NPs in the GAs. The red rings in (d) indicate Fe_3O_4 NPs encapsulated in thin graphene layers. Representative (e) TEM and (f) HRTEM images of Fe_3O_4/N-GAs revealing an Fe_3O_4 NP wrapped by graphene layers.

Scanning TEM (STEM) and elemental mapping analysis of Fe_3O_4/N-GAs suggested the presence of Fe, C, N, and O components in the hybrids (Figure 3a−f). It is notable that the nitrogen content is much higher in the region of Fe_3O_4 NPs than in graphene layers (Figure 3e), indicating that Fe−N−C active sites have been established at the Fe_3O_4 NP interface. X-ray photoelectron spectroscopy (XPS) showed two peaks at 725 and 711 eV, assignable to Fe $2p_{1/2}$ and Fe $2p_{3/2}$ for Fe_3O_4, respectively (Figure 3g and Figure S4).[9] Furthermore, 3.5 wt % nitrogen was estimated to be present in these hybrids on the basis of the XPS analysis. The high-resolution N 1s scan

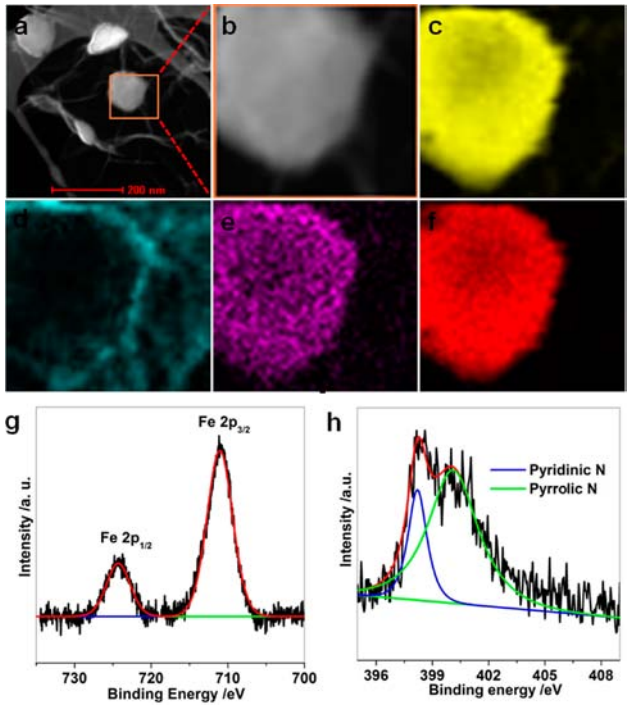

Figure 3. STEM, elemental mapping, and XPS analysis of Fe_3O_4/N-GAs. (a) Typical STEM image. (b) STEM image taken from the square region marked in (a). (c−f) Corresponding elemental mapping images of (c) Fe, (d) C, (e) N, and (f) O. (g, h) High-resolution XPS spectra of Fe_3O_4/N-GAs: (g) Fe 2p; (h) N 1s.

dx.doi.org/10.1021/ja3030565 | J. Am. Chem. Soc. 2012, 134, 9082−9085

(Figure 3h) indicated the presence of two forms of nitrogen, namely, pyrrolic N (401.0±0.2 eV) and pyridinic N (398.1±0.2 eV),[11] both of which have been shown to serve as catalytically active sites for oxygen reduction.[12]

To gain insight into the ORR activity of Fe_3O_4 NPs supported on the 3D macroporous N-GAs, we first examined the electrocatalytic properties of Fe_3O_4/N-GAs in a N_2- and O_2-saturated 0.1 M aqueous KOH electrolyte solution using cyclic voltammetry at a scan rate of 100 mV s^{-1} (Figure 4a).

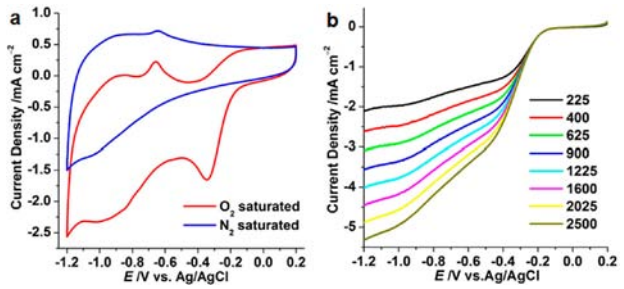

Figure 4. (a) CVs of Fe_3O_4/N-GAs in N_2- and O_2-staturated 0.1 M aqueous KOH electrolyte solution at a scan rate of 100 mV s^{-1}. (b) LSVs of Fe_3O_4/N-GAs in O_2-saturated 0.1 M KOH at a scan rate of 10 mV s^{-1} at different RDE rotation rates (in rpm).

For comparison, we also prepared Fe_3O_4/N-GSs and Fe_3O_4/N-CB via the same procedure (Figures S5–S8). In the case of an Ar-saturated solution, cyclic voltammograms (CVs) within the potential range −1.2 to +0.2 V presented similar features for all three samples. A small redox response at −0.5 to −0.7 V due to the pseudocapacitive behavior of nitrogen-doped carbons was observed (Figure 4a and Figure S6).[13] In contrast, when the electrolyte was saturated with O_2, the three electrodes showed a substantial reduction process. Apparently, Fe_3O_4/N-GAs exhibited a pronounced electrocatalytic ORR activity associated with a more positive ORR onset potential (−0.19 V) and higher cathodic current density (−2.56 mA cm^{-2}; Figure 4a) than for Fe_3O_4/N-GSs (−0.26 V, −1.46 mA cm^{-2}; Figure S6a) and Fe_3O_4/N-CB (−0.24 V, −1.99 mA cm^{-2}; Figure S6b). Subsequently, to examine the reaction kinetics for Fe_3O_4/N-GAs, Fe_3O_4/N-GSs, and Fe_3O_4/N-CB electrodes, linear sweep voltammograms (LSVs) were recorded in an O_2-saturated 0.1 M KOH electrolyte at a scan rate of 10 mV s^{-1} using a rotating disk electrode (RDE) (Figure 4b and Figure S6). Two-step reaction pathways were observed for Fe_3O_4/N-GSs (from −0.26 to −0.62 V and from −0.62 to −1.2 V; Figure S6c) and Fe_3O_4/N-CB (from −0.24 to −0.60 V and from −0.60 to −1.2 V, Figure S6d), suggesting the key role of a two-electron transfer to produce hydroperoxide anions (HO_2^-) as intermediates in alkaline media. In contrast, the LSVs of Fe_3O_4/N-GAs revealed a direct four-electron transfer pathway from −0.19 to −1.2 V for producing OH^- ions (Figure 4b).

To quantify the ORR electron transfer pathway, we employed a rotating ring–disk electrode (RRDE) technique, with which the amount of H_2O_2 generated at the disk electrode could be accurately determined.[12] Figure 5a shows the disk and ring currents for Fe_3O_4/N-GAs, Fe_3O_4/N-GSs, and Fe_3O_4/N-CB, respectively. All three electrodes generated ring currents at the onset potential for the ORR. Notably, both Fe_3O_4/N-GSs and Fe_3O_4/N-CB exhibited much higher ring currents than Fe_3O_4/N-GAs (Figure 5a inset). Specifically, the measured H_2O_2 yield for Fe_3O_4/N-GAs was 11% at a potential of −0.4 V, while those for Fe_3O_4/N-GSs and Fe_3O_4/N-CB were 45 and

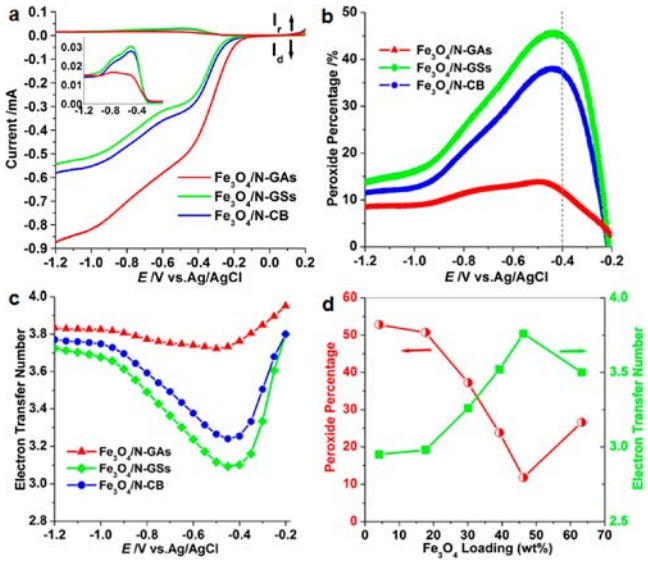

Figure 5. (a) RRDE test of the ORR on Fe_3O_4/N-GAs, Fe_3O_4/N-GSs, Fe_3O_4/N-CB in an O_2-saturated 0.1 M KOH electrolyte at a rotation rate of 1600 rpm. The inset shows the ring current as a function of the electrode potential. (b) Peroxide percentage and (c) electron transfer number of Fe_3O_4/N-GAs, Fe_3O_4/N-GSs, and Fe_3O_4/N-CB as functions of the electrode potential. (d) Peroxide percentage and electron transfer number as functions of Fe_3O_4 loading at −0.4 V, as measured using an RRDE in an O_2-saturated 0.1 M KOH electrolyte.

38%, respectively (Figure 5b). Figure 5c reveals that the electron transfer number varied strongly with the measured potential. On the basis of the ring and disk currents, the electron transfer numbers (n) were 3.09–3.80 for Fe_3O_4/N-GSs and 3.24–3.80 for Fe_3O_4/N-CB over the potential range from −0.20 to −1.2 V. In sharp contrast, the n = 3.72–3.95 for Fe_3O_4/N-GAs electrode over the whole potential range, emphasizing that the Fe_3O_4/N-GAs ORR proceeds mainly via a four-electron mechanism. In view of the similar elemental compositions of the three samples, the enhanced ORR activity of Fe_3O_4/N-GAs can be attributed to the effect of macropores on the diffusion rate of the electrolyte and to the exposed active sites, which are closely related to its high BET surface area (Figure S2) relative to those of Fe_3O_4/N-GSs (Figure S7) and Fe_3O_4/N-CB (Figure S8).

The durability of Fe_3O_4/N-GAs with respect to commercial Pt/C was assessed through chronoamperometric measurements at −0.4 V in O_2-saturated 0.1 M KOH at a rotation rate of 1600 rpm. As revealed in Figure S9, the current–time (i–t) chronoamperometric response for Fe_3O_4/N-GAs exhibited a very slow attenuation with high current retention (79.3%) after 20 000 s. In contrast, a commercial Pt–C electrode showed a much faster current decrease with ~61.0% retention. The better durability of Fe_3O_4/N-GAs can be ascribed to the unique confined structure of Fe_3O_4 NPs within the graphene layers (Figure 2b–f), which can enhance their interfacial contact, suppress the dissolution/agglomeration of NPs, and facilitate the transport of electrolyte ions.[10] The influence of the Fe_3O_4 NP loading on the catalytic activity of Fe_3O_4/N-GAs was also examined using the RRDE. Figure 5d demonstrates that with increasing Fe_3O_4 loading from about 4.1 to 46.2 wt % in Fe_3O_4/N-GAs, the yield of HO_2^- decreased and the overall n value increased from 2.9 to 3.8. However, a high Fe_3O_4 loading of 63.3 wt % in these hybrids resulted in increased HO_2^- production. This can be explained by (i) the decrease in the

dx.doi.org/10.1021/ja3030565 | J. Am. Chem. Soc. 2012, 134, 9082–9085

electrical conductivity of the Fe_3O_4/N-GAs electrode with increasing Fe_3O_4 loading and (ii) the onset of nonbonded interactions with N-GAs for the excess Fe_3O_4 NPs.

Furthermore, we also found 3D N-GAs to be a universal carbon support that is superior to other carbon supports (GSs and CB) for loading of nonprecious metal electrocatalysts. For example, Fe NPs were also successfully incorporated into N-GAs and showed remarkable ORR performance in acidic media (Figures S10−S14 and Table S1).

In summary, we have successfully fabricated 3D monolithic Fe_3O_4/N-GAs hybrids via a combined hydrothermal self-assembly, freeze-drying, and thermal treatment process. Because of the 3D macroporous structure and high surface area, the resulting Fe_3O_4/N-GAs show excellent electrocatalytic activity for the ORR in alkaline electrolytes, including a higher current density, lower ring current, lower H_2O_2 yield, higher electron transfer number (~4), and better durability, potentially making Fe_3O_4/N-GAs a nonprecious metal cathode catalyst for fuel cells. We believe that our present synthetic strategy can be further extended to develop other 3D metal or metal oxide/graphene-based monolithic materials for various applications, such as sensors, batteries, and supercapacitors.

■ ASSOCIATED CONTENT

Supporting Information

Full synthesis and characterization details; AFM image of graphene oxide; N_2 cryosorption isotherm and pore distribution and TGA and XPS data for Fe_3O_4/N-GAs; SEM images, CVs, LSVs, N_2 cryosorption isotherms and pore distributions for Fe_3O_4/N-GSs and Fe_3O_4/N-CB; durability of Fe_3O_4/N-GAs and Pt/C in alkaline solution; XRD, SEM, TEM, EDX, and RRDE data for Fe/N-GAs, Fe/N-GSs, and Fe/N-CB; and durability of Fe/N-GAs and Pt/C in acidic solution. This material is available free of charge via the Internet at http://pubs.acs.org.

■ AUTHOR INFORMATION

Corresponding Author

feng@mpip-mainz.mpg.de; muellen@mpip-mainz.mpg.de

Notes

The authors declare no competing financial interest.

■ ACKNOWLEDGMENTS

Financial support by the Max Planck Society through the ENERCHEM Program, DFG Priority Program SPP 1355, DFG MU 334/32-1, DFG Priority Program SPP 1459, ESF Project GOSPEL (9-EuroGRAPHENE-FP-001), EU Project GENIUS, the BMBF LiBZ Project, and an ERC Grant on NANOGRAPH are acknowledged.

■ REFERENCES

(1) (a) Bashyam, R.; Zelenay, P. *Nature* **2006**, *443*, 63. (b) Lefevre, M.; Proietti, E.; Jaouen, F.; Dodelet, J. P. *Science* **2009**, *324*, 71. (c) Wu, G.; More, K. L.; Johnston, C. M.; Zelenay, P. *Science* **2011**, *332*, 443.

(2) (a) Jaouen, F.; Proietti, E.; Lefevre, M.; Chenitz, R.; Dodelet, J. P.; Wu, G.; Chung, H. T.; Johnston, C. M.; Zelenay, P. *Energy Environ. Sci.* **2011**, *4*, 114. (b) Bezerra, C. W. B.; Zhang, L.; Lee, K. C.; Liu, H. S.; Marques, A. L. B.; Marques, E. P.; Wang, H. J.; Zhang, J. J. *Electrochim. Acta* **2008**, *53*, 4937. (c) Morozan, A.; Jousselme, B.; Palacin, S. *Energy Environ. Sci.* **2011**, *4*, 1238. (d) Su, D. S.; Sun, G. Q. *Angew. Chem., Int. Ed.* **2011**, *50*, 11570.

(3) (a) Zhou, W.; Ge, L.; Chen, Z. G.; Liang, F. L.; Xu, H. Y.; Motuzas, J.; Julbe, A.; Zhu, Z. H. *Chem. Mater.* **2011**, *23*, 4193. (b) Vago, E. R.; Calvo, E. J. *J. Chem. Soc., Faraday Trans.* **1995**, *91*, 2323. (c) Medard, C.; Lefevre, M.; Dodelet, J. P.; Jaouen, F.; Lindbergh, G. *Electrochim. Acta* **2006**, *51*, 3202. (d) Choi, C. H.; Lee, S. Y.; Park, S. H.; Woo, S. I. *Appl. Catal., B* **2011**, *103*, 362. (e) Liang, Y. Y.; Li, Y. G.; Wang, H. L.; Zhou, J. G.; Wang, J.; Regier, T.; Dai, H. J. *Nat. Mater.* **2011**, *10*, 780. (f) Chang, C. H.; Yuen, T. S.; Nagao, Y.; Yugami, H. *Solid State Ionics* **2011**, *197*, 49. (g) Chang, C. H.; Yuen, T. S.; Nagao, Y.; Yugami, H. *J. Power Sources* **2010**, *195*, 5938.

(4) (a) Liu, R. L.; von Malotki, C.; Arnold, L.; Koshino, N.; Higashimura, H.; Baumgarten, M.; Müllen, K. *J. Am. Chem. Soc.* **2011**, *133*, 10372. (b) Charreteur, F.; Jaouen, F.; Ruggeri, S.; Dodelet, J. P. *Electrochim. Acta* **2008**, *53*, 2925. (c) Morozan, A.; Campidelli, S.; Filoramo, A.; Jousselme, B.; Palacin, S. *Carbon* **2011**, *49*, 4839. (d) Chang, C. J.; Deng, Y. Q.; Shi, C. N.; Chang, C. K.; Anson, F. C.; Nocera, D. G. *Chem. Commun.* **2000**, 1355. (e) Chang, C. J.; Loh, Z. H.; Shi, C. N.; Anson, F. C.; Nocera, D. G. *J. Am. Chem. Soc.* **2004**, *126*, 10013.

(5) (a) Liu, R. L.; Wu, D. Q.; Feng, X. L.; Müllen, K. *Angew. Chem., Int. Ed.* **2010**, *49*, 2565. (b) Wang, S. Y.; Yu, D. S.; Dai, L. M.; Chang, D. W.; Baek, J. B. *ACS Nano* **2011**, *5*, 6202. (c) Li, Y.; Zhao, Y.; Cheng, H.; Hu, Y.; Shi, G. Q.; Dai, L. M.; Qu, L. T. *J. Am. Chem. Soc.* **2012**, *134*, 15. (d) Wang, S.; Iyyamperumal, E.; Roy, A.; Xue, Y.; Yu, D.; Dai, L. M. *Angew. Chem., Int. Ed.* **2011**, *50*, 11756.

(6) Wang, Y. J.; Wilkinson, D. P.; Zhang, J. J. *Chem. Rev.* **2011**, *111*, 7625.

(7) (a) Jafri, R. I.; Rajalakshmi, N.; Ramaprabhu, S. *J. Mater. Chem.* **2010**, *20*, 7114. (b) Wang, H. L.; Liang, Y. Y.; Li, Y. G.; Dai, H. J. *Angew. Chem., Int. Ed.* **2011**, *50*, 10969. (c) Seo, M. H.; Choi, S. M.; Kim, H. J.; Kim, W. B. *Electrochem. Commun.* **2011**, *13*, 182. (d) Li, Y.; Wang, H.; Xie, L.; Liang, Y.; Hong, G.; Dai, H. *J. Am. Chem. Soc.* **2011**, *133*, 7296. (e) Li, Y.; Wang, H.; Zhou, J.; Li, Y.; Wang, J.; Regier, T.; Dai, H. *J. Am. Chem. Soc.* **2012**, *134*, 3517. (f) Yan, X. Y.; Tong, X. L.; Zhang, Y. F.; Han, X. D.; Wang, Y. Y.; Jin, G. Q.; Qin, Y.; Guo, X. Y. *Chem. Commun.* **2012**, *48*, 1892. (g) Wu, J. J.; Zhang, D.; Wang, Y.; Wan, Y.; Hou, B. R. *J. Power Sources* **2012**, *198*, 122. (h) Guo, S.; Sun, S. *J. Am. Chem. Soc.* **2012**, *134*, 2492.

(8) (a) Liang, Y.; Wu, D.; Feng, X.; Müllen, K. *Adv. Mater.* **2009**, *21*, 1679. (b) Yang, S. B.; Feng, X. L.; Wang, L.; Tang, K.; Maier, J.; Müllen, K. *Angew. Chem., Int. Ed.* **2010**, *49*, 4795.

(9) Chen, W. F.; Li, S. R.; Chen, C. H.; Yan, L. F. *Adv. Mater.* **2011**, *23*, 5679.

(10) (a) Yang, S. B.; Feng, X. L.; Ivanovici, S.; Müllen, K. *Angew. Chem., Int. Ed.* **2010**, *49*, 8408. (b) Chen, D. Y.; Ji, G.; Ma, Y.; Lee, J. Y.; Lu, J. M. *ACS Appl. Mater. Interfaces* **2011**, *3*, 3078.

(11) Wu, Z. S.; Ren, W. C.; Xu, L.; Li, F.; Cheng, H. M. *ACS Nano* **2011**, *5*, 5463.

(12) Gong, K. P.; Du, F.; Xia, Z. H.; Durstock, M.; Dai, L. M. *Science* **2009**, *323*, 760.

(13) Yang, W.; Fellinger, T. P.; Antonietti, M. *J. Am. Chem. Soc.* **2011**, *133*, 206.